Djath, B.; Schulz-Stellenfleth, J.; Canadillas, B.:

Impact of atmospheric stability on X-band and C-band synthetic aperture radar imagery of offshore windpark wakes

In: Journal of Renewable and Sustainable Energy (2018) AIP

DOI: 10.1063/1.5020437

.

Impact of atmospheric stability on X-band and C-band Synthetic Aperture Radar imagery of offshore windpark wakes

B. Djath,[1, a)] J. Schulz-Stellenfleth,[1, b)] and B. Cañadillas[2]

[1)] *Helmholtz-Zentrum Geesthacht (HZG), Institute of Coastal Research, Germany*

[2)] *UL International GmbH (DEWI), Oldenburg, Germany.*

(Dated: 4 June 2018)

C-band and X-band Synthetic Aperture Radar (SAR) data acquired by the Sentinel-1 and TerraSAR-X satellites are used to study atmospheric wakes behind offshore wind parks in the German Bight. A particular focus is on the impact of atmospheric stability on wake parameters like the wake length. Stability parameters are estimated from measurements taken at the FINO-1 observation platform. Based on a data set covering different seasons and concentrating on the first German offshore wind park Alpha Ventus (AV), it is shown that in this area stable atmospheric conditions favour longer wakes. This is first demonstrated for situations, where the wake behind AV was unperturbed by other neighbor wind parks. In this case wakes of more than 30 km length are observed. In a second step the more complicated situation with wake superposition from different neighboring wind parks is analysed. It is shown that in this case the merged wakes can extend to more than 70 km downstream.

The analysis is challenged by two factors. First of all, the FINO-1 platform is within the wind farm wakes for a certain range of wind directions. This means stability estimates for the upstream conditions are not straightforward to obtain in these conditions. The second complication is associated with an apparent increase of radar cross section downstream of wind parks observed on many SAR scenes, typically within the first 10 km downstream the wind park. A semi-empirical model is proposed to explain this effect by an increased downward momentum flux associated with increased turbulence generated by the wind park. Applying numerical inversion methods, a couple of typical downstream wind speed profiles are reproduced with this model based on SAR derived estimates of the friction velocity.

Keywords: Offshore windfarms, Synthetic Aperture Radar (SAR), Atmospheric stability

[a)] Also at Institute of Coastal Research, Helmholtz-Zentrum Geesthacht (HZG), Germany.

[b)] Electronic mail: Johannes.Schulz-Stellenfleth@hzg.de

I. INTRODUCTION

The wind energy sector has grown rapidly with a global 25% increase each year within the first decade of this century. Projections by the International Renewable Energy Agency (IRENA) estimate that the global use of wind energy will grow by 500% between 2010 and 2030[1]. The wind sector contribution to renewable energy is expected to increase from 2% to 11% during that period. The wind energy production in Germany has reached about 13% of the electricity consumption in 2016. Due to higher mean wind speeds, lower turbulence intensity, as well as the increasing shortage of suitable locations on land, offshore wind farming has become an important factor as a renewable energy source[2]. In 2016 the offshore wind parks (OWPs) installed along the German coast have produced 12.4 GWh, which corresponds to 2.1 % of the electric energy consumption in Germany. By the end of 2016, a total of 947 turbines have been installed and plans for more wind farms exist. Fig. 1 shows some of the major existing and operational OWPs in the German Bight by the end of June 2016.

The growing use of offshore wind resources has led to increased need for information on coastal zone conditions and possible environmental impacts of wind park installations. One important topic in this context is the generation of wakes in the atmosphere, which are potential factors for the operation of neighboring wind farms downstream. In this study such wake effects are investigated using a combination of satellite radar data and in-situ observations.

The extraction of energy and momentum from the wind field by offshore turbines can lead to pronounced wakes downstream. The wake region is generally associated with a velocity deficit, a pressure change and increased turbulence. The length of these wakes can be several tens of kilometers[3,4] and should therefore be considered in the positioning of new installations downstream. The intensity and the extension of wakes is known to depend on different parameters like the atmospheric stability, wind speed as well as wind park size and turbine spacing[3,5,6]. Different observation techniques have been used to study wakes behind wind turbine, e.g., in-situ instruments installed on fixed platforms or wind turbine nacelles (e.g., wind scanner lidars). Measurements from fixed platforms usually provide very good temporal sampling, but lack spatial coverage needed to analyse wake effects on a larger scale. On the other hand, Synthetic Aperture Radar (SAR) systems as flown on the

European SENTINEL-1 or the German TerraSAR-X satellite provide large spatial coverage (up to several hundred kilometers) and high spatial resolution (down to a few meters), but relatively coarse temporal sampling. SAR retrieval of wind information is based on the correlation between the radar cross section and the small cm-scale sea surface roughness.

The overall objective of the study is to improve the interpretation of satellite SAR scenes and to optimise the information extraction concerning offshore wind farm related parameters. The use of SAR for wind speed retrieval is well established and there is a large number of publications about this subject including the radar frequency and polarisation dependence[7–9]. The potential of SAR data to provide information on wind farm wakes has already been demonstrated in previous studies[3–5,8,10]. The first studies on this subject were mainly concerned with the derivation of general wind statistics. These investigations are, for example, related to the optimal siting of offshore wind farms[11,12]. Recently, studies have looked in more detail into the structure and dynamics of offshore wind farm wakes making use of the high spatial resolution of SAR data[4]. First studies were also done considering the impact of atmospheric stability on SAR observed wakes[3].

In this study a couple of new aspects are addressed, which are important for the use of SAR data in the context of offshore wind farm planning and operation, in particular in view of the growing number of installations operating in closer proximity:

- A combination of X-band and C-band SAR data is used for the analysis of offshore wind farm wakes. This approach increases the data basis and adds flexibility compared to the sole use of C-band data in previous studies.

- The dependence of wake parameters on atmospheric stability is investigated for the first operational wind park Alpha Ventus using SAR data in combination with FINO-1 platform measurements and numerical model data. Different parameters quantifying the contribution of thermal stability and wind shear are considered. As a new component an empirical model is fitted relating wake length to stability.

- The superposition of wakes from different wind farms is investigated by analysis of SAR data acquired over Alpha Ventus and the neighbouring Trianel wind park. The data set contains scenes both before and after the Trianel wind farm was installed.

- A semi-empirical model is proposed to explain the increase of radar cross section within

a region of about 10 km downstream of the turbine. The dominant factor in the model is an increased downward momentum flux due to mechanically generated turbulence. The model is required to avoid the misinterpretation of these radar cross section values as increased wind speeds at hub height, which would not make physical sense. This problem, which occurs when applying standard SAR wind speed retrieval schemes to imagery of offshore wind farms, is to our knowledge discussed for the first time.

The manuscript is structured as follows: Section II summarises the basic properties of offshore wind farm wakes and the existing research as well as a short overview of electromagnetic wave scattering from the ocean surface in the microwave regime. The study area and the used data sets are introduced in Section III. The method applied to estimate near surface wind speed from SAR data is described in Section IV. In Section V the results on the impact of stability on wake length and velocity deficit are presented. A semi-empirical model, which is able to re-produce the radar cross section increase immediately behind the wind park is introduced in Section VI.

II. BASICS ON WIND FARM WAKES AND RADAR SCATTERING

A. Offshore Wind farm Wakes

In this study radar images like shown in Fig. 5a,b and Fig. 6a,b are used to analyse wakes downstream of offshore wind farms. The images show wakes of different length behind the wind farm Alpha Ventus (see Fig. 1). In the following we will discuss the interpretation of these radar images and approaches to retrieve useful information about different parameters and processes.

The analysis of wakes behind offshore wind farms has to take into account the particular conditions in the atmospheric boundary layer above the water. Today's offshore wind turbines have typical hub heights of about 100 m and rotor diameters of about 120 m length. These dimensions lead to significant interactions between the turbines and the boundary layer on different spatial and temporal scales.

The understanding of the respective processes is a challenge, because the dynamics is strongly affected by turbulence, which is notoriously difficult to handle both in theory and numerics. The turbulence created by offshore wind farms has typical length scales of 0.5

km[3,13,14]. The situation over water is further complicated by the fact that there is a two-way interaction mechanism between the surface roughness and the wind related friction velocities.

The basic reason for the occurrence of wakes is the removal of momentum by the turbines. The amount of momentum taken out of the boundary layer is depending on the wind speed and the thrust coefficient of the respective turbine[14]. In the first place this leads to an area of reduced wind speed in the downstream area behind the turbines. This reduction then causes wind shear and hence turbulence at the boundary of the wake. The resulting momentum mixing leads to a downstream spread and weakening of the wakes until it finally disappears. The dispersion in the vertical in particular causes the wake to hit the water surface at some distance downstream the turbine. This distance is typically of the order of about 10 rotor diameters[3,15]. The wake dispersion is naturally stronger if there already is a lot of turbulence in the upstream boundary layer. For this reason wakes have a tendency to be more pronounced under thermally stable atmospheric conditions[16]. Another consequence is that wake effects are usually less intense at higher wind speeds (>10 m/s), which are often associated with a higher shear production of turbulence. Exceptions are inversion conditions, where the thermal stability is so strong that high wind speeds can occur with relatively small turbulence intensities.

Wakes have been described by models of different complexity. A simpler 1D model, which basically describes the momentum budget under different stability conditions was proposed by Emeis[16]. Here, momentum is provided from above the turbines and both the turbines and the sea surface act as momentum sinks. Frandsen et al.[15] proposed a parametric model based on the momentum equation, which tries to simulate the spatial structure of wakes including the interaction of wakes from different turbines. Wakes of neighbouring turbines typically merge after about 30 rotor diameters. More complicated 3D simulations are usually done with numerical Large Eddy Simulation (LES) models. One example can be found in Yang, Meneveau, and Shen[17], where also the ocean response is treated in more detail. One problematic issue in the LES models still seems to be the proper representation of turbulence generation, dissipation and advection. Also the level of detail required to describe the interaction of the rotating blades with the airflow is still subject of ongoing research.

Further studies exist on particular aspects of wind turbine wakes, e.g., wake meandering

and survey[18], or the impact on the local and global meteorology[3,19,20].

B. Microwave radar scattering from the sea surface

SAR systems are active radar instruments, which transmit and receive signals in the microwave frequency band. They are thus independent of daylight and are rarely affected by atmospheric conditions (e.g., extreme rain). The measurement of near surface wind speeds from SAR data is based on the so called Bragg scattering mechanism. For a facet tilted by an angle ψ in the x direction and by an angle δ in the y direction the radar cross section associated with Bragg scattering is given by[21]:

$$\sigma_{Bragg}(\theta,\psi,\delta) = 16\pi^4 \cot^4(\theta_i)|\alpha(\theta,\psi,\delta)| \times \Psi\left(2k\sin(\theta+\psi), 2k\cos(\theta+\psi)\sin(\delta)\right) \quad (1)$$

with incidence angle θ, local incidence angle $\theta_i = \cos(\theta+\psi)\cos(\delta)$, electromagnetic wavenumber k, and small scale wave spectrum Ψ. The radar wavelengths for the systems considered here are in X-band (2.5-4 cm) and C-band (4-8 cm). The plane of incidence is in x direction and α is a complex valued function of incidence angle, radar frequency, polarisation and dielectric properties of water. For a surface with various facets tilted in different ways the normalised radar cross section (NRCS) can be estimated as

$$\sigma^0 = \int \frac{\sigma_{Bragg}(\theta,\psi,\delta)}{\cos\psi\cos\delta}\, p(\tan\psi,\tan\delta)\; d(\tan\delta)d(\tan\psi), \quad (2)$$

where $p(\tan\psi,\tan\delta)$ is the slope probability density function. This function can be derived from the ocean wave spectrum Ψ.

Based on dimensional considerations it can be shown that the high frequency ocean wave spectrum appearing in eq. 1 is of the following form

$$\Psi(k,\phi) = k^{-4} f(\phi, ku_*^2/g), \quad (3)$$

where f is an unknown function[22], u_* is the friction velocity and g is the acceleration of gravity. Eqs. 1-3 show that there is a direct connection between the normalised radar cross section σ^0 and the friction velocity u_* for a given wind direction. Making assumptions about the shape of the short wave spectrum, analytical models can be derived for the simulation of σ^0 from given wind conditions. Because these models still contain a lot of uncertain

components, empirical models are often preferred for practical applications like wind speed retrieval from radar. A recent comparison of physically-based and empirical models can be found in Fois[23].

As empirical models already exist for C-band and X-band, which are suitable for the incidence angle regimes of Sentinel-1 and TerraSAR-X data, we will follow this approach here. More details on how these functions were used for the wind speed retrieval in this study are given in Section IV A.

III. STUDY AREA AND USED DATA SETS

A. The offshore wind park Alpha Ventus

The present study is focused on the offshore wind park Alpha Ventus (AV). Starting operational production in April 2010, AV was the first offshore wind park at the German Coast. AV is located approximately 45 km north of the island Borkum and about 400 m east of the observation platform FINO-1 (see Fig. 1). More details on this platform will be given in Section III C. The offshore wind park consists of twelve 5-megawatt turbines, which are arranged in 3 columns and 4 rows with a spacing between 761 m and 849 m. The wind turbines have hub heights of about 90 m and rotor diameters of about 120 m. The cut-in wind speed of the turbines is ∼3.5 m/s, while the rated wind speed is 13 m/s. At strong wind speeds between 25-30 m/s, the turbines are shut down for safety reason. AV covers an area of about 4 km^2 and is surrounded by neighbouring OWPs, such as Borkum Riffgrund installed in 2014 (∼ 2-4 km to the South) and Trianel installed in June 2014 (∼5-10 km to the west) (see the zoom in area in Fig. 1).

B. TerraSAR-X and Sentinel-1 data sets

TerraSAR-X was launched on 15 June 2007[24]. It flies at a sunsynchronous orbit at 514 km altitude with an exact repeat cycle of 11 days. It has three acquisition modes (Spotlight, StripMap and ScanSAR) with different polarisations such as VV, HH, VH, HV depending on the image mode. The StripMap and ScanSAR data used in this study have a spatial resolution of about 3 m and 18 m respectively and the across track image width is about 30 km for StripMap and 100 km for ScanSAR.

The ESA SAR data used in this study were acquired by the Sentinel-1A satellite launched on 3 April 2014[25]. The satellite also flies on a sunsynchronous orbit at about 800 km altitude. The exact repeat cycle is 12 days. The instrument has four acquisition modes (Strip Map, Interferometric Wide Swath, Extra-Wide Swath and Wave-Mode). The data used in this study were acquired in Interferometric Wide Swath mode, which provides images with across track width of about 250 km. The high resolution products provided in this mode have a resolution of about 20 m. This instrument also gives four possibilities for polarisation (VV, HH, VH, HV). In our study, vertical polarization for transmission and reception (i.e., VV) is used. VV is traditionally preferred for SAR wind speed retrieval, because of the higher NRCS (see eq. 2) obtained with this polarisation for the sea surface. It should be noted that additional SAR products exist that could potentially improve wind speed estimates. For example, TerraSAR-X has a fully polarimetric mode and SENTINEL-1 provides additional maps of Doppler centroid estimates, that can be linked to near surface wind speeds[26,27]. The respective methods and theories are however less consolidated than the techniques used in this study and were therefore left for consideration in future studies.

Due to the sunsynchronous orbits of both satellites, data are always taken around the same time of the day. For the German Bight the TS-X and Sentinel-1A acquisitions are around 05:00 UTC and around 17:00 UTC.

Satellite	Band	Frequency [Hz]	wavelength [m]	Rep. Cyc. [days]	Resol. [mxm]
TerraSAR-X	X	9.6 GHz	0.031 m	11	3 m × 3 m
					18.5 m × 18.5 m
S1A	C	5.4 GHz	0.055 m	12	20 m × 22 m

TABLE I. Some relevant imaging parameters for TerraSAR-X and S1A.

C. FINO-1 data

FINO-1 is a research platform installed at 54°N, 6°E 35' in the North Sea[28], which is about 400 m west of the Alpha Ventus offshore wind park. It is devoted to measure meteorological and oceanographical parameter for research purposes. Air temperature is measured at 30

Dates [yyyymmdd]	Time [UTC]	Satellite
20110807	17:18	TS-X
20120826	17:18	TS-X
20120510	05:59	TS-X
20120418	05:59	TS-X
20140120	17:10	TS-X
20140122	05:51	TS-X
20140420	05:50	TS-X
20150512	05:49	S1-A
20150522	17:16	S1-A
20150527	17:25	S1-A
20150603	17:16	S1-A
20150605	05:49	S1-A
20151018	17:25	S1-A
20151030	17:25	S1-A
20151111	17:25	S1-A
20151123	17:25	S1-A
20151212	17:16	S1-A
20160307	05:49	S1-A
20160310	17:25	S1-A
20160322	17:16	S1-A
20160329	17:16	S1-A
20160516	17:16	S1-A
20160528	17:16	S1-A

TABLE II. List of TerraSAR-X and S1A scenes with wake features used in this study.

m, 40 m, 50 m, 70 m, and 100 m height, while wind speed measurements are taken at 33 m, and from 40 m to 100 m height in 10 m steps. The wind direction is also measured at 33 m, and from 40 m to 90 height every 10 m steps. These parameters are provided every 10 minutes. Hourly measurements for water temperature at 3 m, 6 m, 10 m, 15 m, 20 m and 25 m depths are provided and Sea Surface Temperature (SST) measured by a directional waverider buoy[28] at 0.5 m depth is delivered every 30 min.

FINO-1 observations were not available for all satellite acquisitions, and in order to fill these gaps numerical model data described in the next section were used in addition.

D. Auxiliary dataset

The German Weather Service (DWD) provides hourly weather data based on observations and numerical models. The variables available for our study were SST, air temperature at 2 m above the sea surface (T_a), and the wind vector at 10 m height. The data originate from

the icosahedral nonhydrostatic (ICON) model and were provided on a 1/16° grid. It was found that overall the DWD parameters are in good agreement with the FINO-1 observations confirming previous studies[29].

The distribution of wind conditions at the time of the satellite acquisitions used for wake analysis in this study are shown in Fig. 2. It can be seen that these scenes, which all show wake features, cover a wide range of different wind directions and wind speeds. The satellite data also represent different seasons with a slightly stronger weighting of the summer half-year. This has to do with the higher probability of stable atmospheric conditions in this period, which favours the formation of wakes, as discussed in the following sections.

IV. METHODS

A. SAR wind speed retrieval

For the radar wavelengths and incidence angles of typical SAR instruments like TerraSAR-X or Sentinel-1 the Bragg wavelengths appearing in eq. 1 are of the order of a few centimeters (see table II). Because the energy on this roughness length scale is highly dependent on the near surface wind, these radar instruments allow the retrieval of wind speed information. The method that enables the conversion of the NRCS to near surface wind speed is based on a so called geophysical model function (GMF), which is an empirical model originally developed for scatterometer wind vector retrieval[30–33]. Two different GMFs have been used for TerraSAR-X and Sentinel-1 scenes as the NRCS depends on the radar frequency. For C-band and VV polarization, the CMOD5 GMF[34] has been used. As it has been found from statistical studies that CMOD5 GMF underestimates retrieved wind speed by roughly 0.5 m/s[35], the updated version CMOD5.N GMF[36] is employed for this study. CMOD5.N GMF provides 10 m wind speed at neutral conditions while avoiding errors related to atmospheric stratification. Similarly to CMOD5, X-MOD2 GMF has been tuned and adapted for X-band frequency by Li and Lehner[37]. Both GMFs are valid for incidence angles between 20-45° and share the same functional form given by[34,37]

$$\sigma^0 = B_0(1 + B_1 \cos\phi + B_2 \cos 2\phi)^{1.6}, \tag{4}$$

where B_0, B_1 and B_2 are functions of wind speed and incidence angle, and ϕ is the angle between the wind direction and the SAR look direction.

In practice, the wind speed retrieval requires some prepossessing of data such as the radiometric calibration to σ^0. Both C-band and X-band scenes were calibrated to σ^0 using the SNAP software tool[38] provided by the European Space Agency (ESA).

According to eqs. 1 and 2 the radar cross section is depending on the 2D small scale slope distribution, which in turn is a function of the 2D wind vector. The inversion of eq. 4 therefore requires knowledge about the wind direction. There are approaches to obtain wind direction information from SAR images[39,40], however with the additional presence of wakes and radar signatures from wind turbines[41], the application of such methods to the scenes analysed in this study is not straightforward. Also, there is no guarantee that the image features required for the application of this method are actually present in the SAR scenes. For this reason we have made additional use of wind direction information from the operational German Weather Service (DWD) forecast model (see Section III D). It should be emphasized that this is of course a significant simplification, because possible wind direction changes on a smaller scale within the wake area are neglected. The general sensitivity of SAR wind speed measurements to wind direction errors was discussed in previous studies[9]. We do not discuss this point in more detail here, because of the lack of independent information on wind direction within the wake area. The overall good agreement of the alignment of different SAR image features like atmospheric boundary rolls with wind directions from atmospheric models was demonstrated in previous studies[42]. Different problems encountered when comparing numerical models with observations at higher resolutions were discussed in earlier publications[43–45].

Another issue is the so called speckle noise, which can deteriorate SAR wind speed estimates, if very small spatial scales are considered[7]. A usual way to remove the speckle noise is to block-average the NRCS to coarser resolutions[39], i.e., the calculated wind speed cells have a larger size than the initial NRCS cells. In our study the available SAR data were smoothed down to a resolution of about 200 m both in azimuthal and range direction. This approach is consistent with previous studies[37,39] and represents a reasonable compromise between speckle noise reduction and preservation of spatial resolution required to analyze offshore wind farm wakes.

The empirical models discussed above are tuned to 10 m wind speed for practical reasons. However, as explained in Section II B, the radar cross section is actually closer related with the friction velocity u_*, which describes the stress at the water surface[33]. The relationship

of u_* and U_{10} is of relevance for the discussions to follow and is therefore briefly addressed.

A first estimate of u_* can be obtained by assuming neutral conditions, where the wind speed profile is given by

$$u(z) = \frac{u_*}{\kappa} \log(\frac{z}{z_0}), \tag{5}$$

with Karman constant κ and roughness length scale z_0. Using the Charnock equation

$$z_0 = 0.015\ u_*^2/g \tag{6}$$

to relate z_0 to u_*, one obtains an implicit equation for the friction velocity given a wind speed at a certain height z.

By combination of a GMF with eqs. 5, 6, one obtains a relationship between friction velocity and normalised radar cross section as illustrated in Fig. 3. The curves correspond to X-band (dotted lines) and C-band (solid lines) for different incidence angles (20°, 30° and 40°) with the antenna looking in the upwind direction. The radar cross section increases with growing friction velocity and decreases with growing incidence angle.

Fig. 3 also gives an idea about the relevance of the radiometric accuracy of the SAR instruments. The absolute radiometric accuracy for both SAR systems is reported to be around 0.5dB[46,47]. For example, for C-band, 30° incidence angle, and u_*=0.3 ms^{-1} this would result in an absolute error of about 10% (see Fig. 3). One has to take into account however, that for the analysis performed in this study the relative accuracy, which is usually higher than the absolute accuracy, is of more significance. From Fig. 3 one can see that the sensitivity of wind estimates with respect to radiometric errors is higher at very high speeds. However, the very high wind speed regime is not of interest for this study anyway, because wind turbines are switched off in those conditions.

B. Image selection procedures

This study concentrates on a data set of SAR scenes collected both from X-band (TerraSAR-X) and C-band (Sentinel-1A) radar in VV polarisation. The main reason for this choice of polarisation is that the commonly GMFs were tuned to radar data acquired in this mode. Furthermore, the GMFs are known to be applicable only within an intermediate incidence angle range of approximately 20° to 65°. Apart from these restrictions on radar parameters, the following selection criteria were used:

- The scene contains the offshore wind park Alpha Ventus.
- The scene shows a wake feature behind the wind park.
- The major part of the wake feature is contained on the image.
- The scene is not affected by strong modulations of the radar cross section, which are not related to wakes, e.g., associated with convective cells or atmospheric fronts.

Wakes downstream offshore wind farms lead to characteristic modulations of the mormalised radar cross section visible on SAR imagery; for instance, shadow areas in NRCS indicate reduced wind speed (see Fig. 4). Unlike the ocean circulation effects for the Horns Rev wind park discussed in Hasager et al.[11], the bathymetry of the Alpha Ventus site is relatively uniform and also farther offshore, i.e., ocean current related phenomena are expected to be very weak. Also, NRCS modulations associated with ocean currents should show a strong alignment with the tidal currents. This could not be observed for the analysed data set, where the alignment was clearly dominated by the wind direction. Out of 180 scenes, which contain the wind park Alpha Ventus, 61 images showed wake features. In 42 cases the complete wake was on the image allowing a wake length estimation. From this data set 9 images had to be dropped, because of strong background variations of the wind field (e.g., convective cells, boundary layer rolls), which did not allow a reasonable estimation of reference wind speed profiles. Another 10 cases had to be discarded, because insitu information on atmospheric stability was not available. In the end, 23 wake scenes were available for the analysis. As will be shown in following, this relatively small data set was sufficient to establish a relationship between atmospheric stability and wake length.

C. Stability parameter estimation technique

In this section the techniques to quantify the stability of the atmospheric boundary layer are described. Basically, the considered parameters quantify the relative role of two mechanisms: thermal stratification, which dampens turbulence; velocity shear, which creates turbulence. One of the standard parameters used in this context is the Monin-Obhukhov length scale L, which is defined as

$$L = -\frac{\theta_v u_*^3}{\kappa g \overline{w'\theta_v'}} \,, \tag{7}$$

where θ_v is the potential virtual temperature and $\overline{w'\theta'_v}$ is the vertical flux of potential virtual temperature. When $L < 0$, the surface layer is statically unstable, and when $L > 0$ the surface layer is statically stable. The absolute magnitude of L indicates the deviation from statically neutral state, with smaller $|L|$ values corresponding to larger deviations from neutral conditions. When L is negative and $|L|$ is small, buoyant processes dominate the production of turbulent kinetic energy compared with shear production. For neutral conditions one has $L \to \infty$. Based on the Monin-Obhukhov length the non-dimensional stability parameter η defined by $\eta = z/L$ with a given reference height z is often used in the literature.

In practice the momentum and heat fluxes in the definition of L are hard to estimate. For this reasons there are approximations for η based on the bulk Richardson number, which is easier to obtain from observations commonly available. The bulk Richardson number as used in Christiansen and Hasager[3] and Hansen et al.[48] is given by

$$R_{ib} = \frac{g}{T_2} \frac{\frac{T_2 - T_1}{z_2 - z_1} + 0.01 \, \frac{\mathrm{K}}{\mathrm{m}}}{(U_z/z)^2}, \tag{8}$$

where g is the acceleration of gravity, $T_2 - T_1$ the absolute temperature difference at two levels $z_2 > z_1$, and U_z is the wind speed at z. If the vertical gradient of absolute temperature is equal to the dry adiabatic lapse rate (≈ -0.01 K/m), the atmosphere is regarded as neutral and $R_{ib} = 0$.

The stability parameter can be estimated from this according to[49]

$$\eta = 10 \, R_{ib} \quad \text{for unstable conditions, i.e.,} \quad L_* \leq 0 \tag{9}$$

$$\eta = \frac{10 R_{ib}}{1 - 5 R_{ib}} \quad \text{for stable conditions, i.e.,} \; L_* > 0 \tag{10}$$

As indicated by eq. 8, the Bulk Richardson number R_{ib} can be computed from a difference of observed temperature at two levels and a single observed wind speed. In this study eq. 8 was used with $z_1 = 0$, i.e., T_1 is the sea surface temperature (SST). Based on this approach the stability parameter η has been computed using hourly data sets from the FINO-1 platform. The hourly measurements of wind speed, air temperature, water temperature, and sea surface temperature represent 10-minutes averages. For the absolute temperature T_2 and the wind speed U_z in eq. 8 the FINO-1 measurements at 50 m have been used.

In case there is no meteorological data sets from FINO-1 available, another possibly rough estimation of stability conditions can be obtained from weather maps[50] and SST from DWD.

The use of SST from DWD was only necessary for the scene on 30 October 2015. The air temperature from the weather maps was applied for the scene on 22 May 2015 and was kept separate in the statistical analysis for consistency reasons.

V. STABILITY DEPENDENCE OF WAKE LENGTH

A. Wake length by velocity deficit estimation

Wind speeds over the coastal ocean can show strong variations for many different reasons like, e.g., atmospheric fronts. Another typical phenomenon is the increase of wind speed with growing distance from the shore (Fig. 4a). The basic reason for this effect is the smaller surface roughness of the sea compared to land. In the coastal transition area between these two roughness regimes an internal boundary layer is formed, in which different adjustment processes concerning momentum, heat and moisture fluxes take place[51]. In many cases this effect leads to a significant NRCS increase from land to sea visible on SAR images[3]. A typical example is shown in Fig. 4, which displays a strong South-North wind speed gradient characterized by mean wind speed less than 6 m/s in the area South of AV wind park, while wind speed greater than 8 m/s are found in the northern part.

The velocity deficit V_d defined as

$$V_d(x) = \frac{U_{freestream}(x) - U_{wake}(x)}{U_{freestream}(x)} \tag{11}$$

with downstream distance x from the wind farm is an important parameter for the wake analysis. The $U_{freestream}$ component is defined as the unperturbed wind upstream the wind turbines, while U_{wake} is the wind speed in the wake downstream the wind turbines. The use of a single value for $U_{freestream}$ representing the upstream conditions may introduce significant errors in the computation of V_d due to non-homogeneous spatial variations of NRCS associated with the background wind field. To overcome this problem, another reference has been considered. The $U_{wake}(x)$ estimate for a certain distance x from the wind farm is obtained by averaging across the wake. The background wind field $U_{freestream}(x)$ required to estimate the wind speed deficit is obtained from an area parallel to the wake. The application of this method to the Sentinel-1 scene acquired on 30 October 2015 is illustrated in Fig. 4b. The row of boxes on the right represents the background variations of the wind field, whereas the row on the left is located downstream of the offshore windpark and covers the

wake. This method is similar to that used in Christiansen and Hasager[3,5], where $U_{freestream}$ becomes dependent on the downstream distance as well. The length of each small box is 2 km and the spatial mean of wind speed for each box is used for the computation of V_d. The wake length is here defined as the distance from the wind farm, where the deficit V_d changes from positive to negative sign. It is important to note, that it is not sufficient to look for general zero crossings of V_d, because quite often there is a zero crossing of the deficit going from negative to positive values at a distance of about 10 km, which is associated with bright radar signatures discussed in more detail in Section VI. It should also be noted that the fact that the analysis is based on a relative quantity (velocity deficit) makes the results quite robust with respect to errors in absolute wind speed estimates, e.g., due to errors in the GMFs or radiometric calibration.

B. Downstream wake length and velocity deficit and stability dependence

The 4 SAR images in Fig. 5a,b and Fig. 6a,b evidently show wake patterns. They were acquired under thermally stable and neutral conditions (see table III). The atmospheric stability condition is determined using eq. 8 and in-situ data. For the image acquired on 22 May 2015, the thermal stability was derived from the difference between the air temperature from the Berliner Wetterkarte[50] and the SST from FINO-1 due to data gaps in FINO-1 air temperature data. The analysis of the wind turbine wake downstream is focused on the wake starting at the Alpha Ventus offshore wind park (AV). Figs. 5a,b represent situations, where the wakes are caused by AV alone, while in Figs. 6a,b the wake downstream AV is influenced by other nearby OWPs, such as Borkum and Trianel.

The latter situation with the superposition of wakes originating from different wind parks is naturally more complex. In the following we therefore take a two step approach, where isolated wakes are considered first.

1. Isolated wakes

The cases where an isolated wake without interference with other OWPs is found behind AV are referred to as "AVa" in the following. Figs. 5a,b show a TS-X scene acquired on 10 May 2015, 05:59 UTC and a Sentinel-1 scene acquired on 30 October, 17:25 UTC. For

449 the TS-X image (Fig. 5a) the wind was from the southerly directions and this time the
450 wake signature is characterized by increased σ^0 values in the downstream direction. This
451 unexpected behavior will be addressed in more detail in Section VI. For the Sentinel-1 image
452 (Fig. 5b) the wind was coming from south easterly direction and 2 zones with low amplitude
453 of σ^0 (about -20 to -18 dB) can be seen downstream of the wind parks AV and the group
454 of wind parks comprised of Borkum Riffgrund and Trianel. In the first case the wind is
455 approximately parallel to the wind turbine rows and 3 distinct wake patterns are observed
456 downstream, before they are merging about 3.6 km from the wind farm, which represents
457 $\sim$30D, where D$\approx$120 m is the rotor diameter. This observation is consistent with the study
458 presented in Frandsen et al. [15], where this is explained by lateral dispersion of the individual
459 wakes. In Fig. 5b the situation is different, because the wind is oblique to the rows of the
460 winds turbines and the cross section of the resulting superposition has a more homogeneous
461 cross section.

462 The corresponding near-surface U_{10} wind fields obtained with the method described in
463 Section IV A are shown in Fig. 5 c,d. For the Sentinel-1 image taken on 30 October 2015 the
464 estimated wind speed within the wake is about 7 m/s. The wind speed in the background
465 wind field is around 2 m/s higher. For the TS-X image acquired on 10 May 2012 the
466 estimated wind speed within the wake is around 9 m/s and thus about 2 m/s higher than
467 in the background wind field. Again, this unexpected behaviour is analysed in more detail
468 in Section VI.

Using the technique described in Section V A, the wake lengths were estimated as 32 km for the TS-X scene (Fig. 5a) and 28 km for the Sentinel-1 scene (Fig. 5b). The corresponding velocity deficit curves as a function of the distance from the AV wind park are plotted in grey in Fig. 7a. Considering the atmospheric conditions for both scenes, the longest wake is found for the more stable case on 10 May 2012 (Fig. 5a) with air/sea temperature difference of more than 5°C (table III). The corresponding maximum velocity deficit is approximately 5% (Fig. 7a). For the Sentinel-1 scene the conditions were close to neutral with air/sea temperature difference of about 1°C. The observed vertical profile of temperature (and wind speed) from the FINO-1 platform for the case from 30 October 2015 is shown in Fig. 5f and indicates the instability of the atmosphere. In this case the velocity deficit is about 6%. It should be mentioned that a considerable number of these FINO-1 wind profiles have a quite complicated structure, which only in a coarse approximation follow a simple log law. This

issue has been the subject of previous studies[52]. It is interesting to note that the bright features characterised by negative deficit values in Fig. 7a occur in the more stable situation with higher air/sea temperature difference. This issue will also be addressed in Section VI. The analysis was extended to 8 SAR scenes showing isolated wakes behind AV. The data cover a wide range of thermal stability conditions, i.e, from stable to unstable. A scatter plot showing the temperature gradient and the wake length on the horizontal and vertical axis can be found in Figs. 5e. The linear regression line is given by

$$\lambda_{wakes} = 19.5\ \mathrm{km} + 95200\,\frac{\mathrm{m}^2}{\mathrm{K}}\,\frac{\partial\theta}{\partial z} \tag{12}$$

with wake length λ_{wakes}. It can be seen, that longer wakes are found in neutral and stable conditions, whereas shorter wakes are associated with unstable conditions.

2. Superimposed wakes

The cases where a superposition of wakes from different OWP is observed are referred to as "AVa+" in the following. The potential influence of the Borkum and Trianel wind farms on Alpha Ventus is illustrated in Fig. 6. In the Sentinel-1 scene taken on 22 May 2015 (Fig. 6a) the wind is from the south west and AV is within the wake of the Borkum OWP, which is less than 5 km to the west. The atmospheric stability during the acquisition time was quite high with an air/sea temperature difference of almost 4°C (see table III). The corresponding SAR derived wind field is shown in Fig. 6c. The wake length estimated for this case is about 68 km and the corresponding maximum velocity deficit is approximately 20%.

On the Sentinel-1 image acquired on 28 May 2016 (Fig. 6b), the wind is in the opposite direction compared to the previous case, i.e., from the north east. The image shows bright features downstream AV before crossing Borkum wind farms. The scene was taken under stable conditions with air/sea temperature difference of almost 1.1°C. The stability conditions can also be appreciated from the vertical profile of the temperature (Fig. 6f). The wake length estimated for this case is about 70 km and the maximum velocity deficit is about 16%.

The corresponding velocity deficit curves as a function of the distance from the AV wind park are plotted in black in Fig. 7a. It is evident that the two cases with superimposed

wakes lead to more pronounced deficits and longer wakes. Furthermore, it can be seen as in the previous examples (AVa) that the bright features immediately downstream AV are more pronounced in the stable situation on 22 May 2015.

A total of 15 SAR scenes were used for the analysis of "AVa+" scenarios with superposition of wakes. The longer wakes are identified in neutral and stable conditions, whereas shorter wakes are found in unstable conditions (Fig. 6e). This case is more complex than previously, because some scenes in unstable conditions display longer wake length than those in neutral or thermally stable conditions. The difference of the wake length for the same class of stability could be due to some parameters such as the number of wind turbines as well as the layout of the wind farm, the wind speed and the wind direction. The wake length is longer than in "AVa", which could suggest that the number of wind turbines influence the extension of the wake length. In a consistent manner as in the "AVa" cases, the dependence of V_d on the stability is not clearly established (Fig. 7a). This is also not surprising because, at least at hub height, the maximum deficit is expected to occur immediately downstream the wind park and should mainly depend on the thrust coefficient of the turbines and the wind speed[53]. Nonetheless, for the unstable cases, the maximum of V_d is identified relatively in the first 10 km, while shifted further away from the hub for neutral and stable situations. Higher velocity deficit values are found for these complex cases.

Another issue to be considered is the shadowing of the FINO-1 platform by AV[54,55]. For easterly wind directions the presence of AV leads to increased turbulence levels and reduced wind speeds compared to unperturbed conditions. Reduced wind speeds increase the magnitude of the Richardson number and hence the stability parameter $\eta = \zeta/L$ (eq. 8). The effect of AV on the temperature gradients measured at FINO-1 is more complicated. It seems to be reasonable to assume that the turbulence introduced at hub height and generated by the rotors leads to downward vertical mixing and thus affects the air temperature at 50 m (height at which measurement is taken for our analysis) and below. This means that the magnitude of the temperature difference between 50 m and sea surface will be biased. In fact, for stable conditions, where the upper warm air flows over the cold air, the vertical mixing will bring the warm air down and the cold air up. This will lead to an increase of temperature in the lower layer and therefore reduced temperature gradient. For unstable conditions, the effects will be the other way around. The unstable cases with south-/north- easterly wind direction shown in Fig. 7b could in fact fall into this category. It is obvious that a correction

of these cases towards more neutral conditions would lead to a better consistency with the other cases shown in the plot. This also applies to the two longest wakes in Fig. 7b in neutral and slightly stable conditions, which should be moved towards more stable conditions for a more suitable correlation between the stability and wake length. For instance the correction for the case on 28 May 2016 could increase the thermal stratification difference and hence the vertical gradient on the profile of the temperature (Fig. 6f). The case on 30 October 2015 in Fig. 5a (represented by the green dot) could be moved also to the right side of the plot and its temperature profile improved.

Dates (yyyymmdd)	Satellites	Air temperature T_a ($^\circ C$)	SST ($^\circ C$)	Wind speed at FINO (m/s)	Wind direction	Atmospheric stability	Wake length (km)	Velocity deficit (%)
20120510	TS-X	13.9	8.7	14.7	162.9	Stable	32	5
20150522	S1A	15	11.2	9	239.5	Stable	68	20
20151030	S1A	12	13	8.7	137.5	Slightly unstable	28	6
20160528	S1A	13.6	12.5	7.4	47.2	Stable	70	16

TABLE III. Wake and atmospheric parameters for four SAR data cases shown in Fig. 5a,b, and Fig. 6a,b.

VI. TURBULENCE RELATED SAR SIGNATURES

In this section a model is proposed to explain the radar cross section variations seen on SAR images of wakes behind offshore wind turbines. The most interesting feature addressed in this context is the increase of normalized radar cross section within a distance of typically 10 km behind the turbines (e.g., Fig. 5a and Fig. 6a), which is found in about one quarter of the SAR scenes with wake features. This feature usually occurs in combination with a darker wake signature observed downstream of the bright features until the background cross section level is regained.

These observations seem to be quite paradox at first sight, because a naive application of standard SAR wind speed retrieval algorithms to imagery within a couple of kilometers downstream of offshore wind parks could lead to the unphysical conclusion that there is a general increase of wind speed up to hub height in this area. The proposed model is supposed to be a help for users of SAR data in the offshore wind context to avoid this misinterpretation.

According to the standard theory the radar cross section should be dominated by Bragg scattering at least for the typical incidence angles considered in this study. As explained in Section II B the cross section is therefore for the most part controlled by the friction velocity u_*. The friction velocity in turn is highly dependent on the wind speed at higher levels, the vertical mixing length scales associated with turbulence, and the ocean surface roughness. For the roughness parameter z_0 a first order formulation is given by the Charnock relation eq. 6. This is an approximation, because there is actually also a wave age dependence, which we neglected in this first approach[56]. In the Prandtl layer (typically first 100 m) we have

$$u_* = \frac{du}{dz} l \tag{13}$$

with the mixing length scale $l = \kappa z$ according to the law of the wall. This results in the classical log wind profile for neutral conditions eq. 5, which is characterised by a constant momentum flux in the vertical. In non-neutral conditions it is usually assumed that the mixing length scale is modified according to $l = \kappa z/\Phi$. Here, Φ is a dimensionless stability function depending on z/L, where L is the Monin-Obukhov length scale. We then have

$$u_* = \frac{du}{dz} \, \frac{\kappa z}{\Phi(z/L)} \, . \tag{14}$$

Based on the analysis of experimental data, the following form for the stability function is most often used in the literature[51]:

$$\Phi(z/L) = \begin{cases} 1 + 5 \; z/L \;\; \text{for} \;\; z/L \geq 0 \\ (1 - 16 \; z/L)^{-1/4} \;\; \text{for} \;\; z/L < 0 \end{cases} \tag{15}$$

To find a solution for u in eq. 14 the function $(1 - \Phi(z/L))/z$ is integrated over z yielding

$$\psi(z/L) = \begin{cases} -5 \; z/L + \beta_1 \;\; \text{for} \;\; z/L \geq 0 \\ 2\ln((1+x)/2) + \ln((1+x^2)/2) \\ -2\tan^{-1}(x) + \frac{\pi}{2} + \beta_2 \;\; \text{for} \;\; z/L < 0 \end{cases} \tag{16}$$

with $x = (1 - 16z/L)^{1/4}$ and constants β_1, β_2. We then get

$$u(z) = \frac{u_*}{\kappa} \big(\ln(\frac{z}{z_0}) - \psi(z/L) \big) \;\; . \tag{17}$$

The constants are chosen such that $\psi(0) = 0$, which leads to $\beta_1 = \beta_2 = 0$. Because z_0 is small, we then also have $u(z = z_0) \approx 0$ [51].

The idea in this study is to define a new stability function, which takes into account the turbulence mechanically generated by the wind turbines. As already pointed out before, wakes occur predominantly in stable atmospheric condition. For this reason, we use the formulation for stable conditions in eq. 15 as a basis and define

$$\Phi^{WT}(z) = 1 + \; z \; \frac{\Phi^{hub} - 1}{H^{hub}} \;\; \text{for} \;\; z \leq H^{hub} \tag{18}$$

with a mixing length correction factor Φ^{hub} at hub height, which has to fulfill

$$0 < \Phi^{hub} \leq 1 + 5 \; H^{hub}/L \tag{19}$$

in order to increase the mixing length with respect to neutral conditions. With this stability function the mixing length behind the wind turbine is increased by a factor of $1/\Phi^{WT}$. The respective profile then follows as

$$u(z) = \frac{u_*}{\kappa}\Big(\ln(\frac{z}{z_0}) + (z - z_0) \; \frac{\Phi^{hub} - 1}{H^{hub}}\Big) \; , \tag{20}$$

where we imposed the boundary condition $u(z_0) = 0$.

The parameter Φ^{hub} describes the impact of the turbulence generated by the turbines on the vertical momentum fluxes. This turbulence dissipates in the downstream direction and therefore the length scales will slowly go back to their original value in the background wind field. Denoting by x the downstream distance from the turbine we formulate this process as

$$\Phi^{hub}(x) = e^{-x^2/\sigma_{turb}^2} \; \Phi^{hub} + \Big(1 - e^{-x^2/\sigma_{turb}^2}\Big)\Big(1 + 5 \; H^{hub}/L\Big) \tag{21}$$

with an e-folding distance σ_{turb} after which the mixing length increase has dropped to about one third.

At the same time the mean wind speed U is reduced by a factor $R_0 = U/U_0$ behind the wind turbine and recovers to the original value U_0 after some distance downstream. Following the derivation of Betz law, which is based on the consideration of momentum and energy conservation, this factor is related to the thrust coefficient c_T via[15]

$$R_0 = \sqrt{1 - c_T} \; . \tag{22}$$

Here, the thrust coefficient is used to relate wind speed U and air density ρ to the force F experienced by a turbine with rotor disc area A according to[15]

$$F = 0.5 \, \rho \, A U^2 c_T \;\; . \tag{23}$$

The thrust coefficient itself is a function of wind speed as well. An empirical relationship to estimate the thrust coefficient from the wind speed is given by[53]

$$c_T = \frac{3.5\frac{\mathrm{m}}{\mathrm{s}}\,(2\,U - 3.5\frac{\mathrm{m}}{\mathrm{s}})}{U^2}\,. \tag{24}$$

For the downstream evolution of the wind speed reduction factor R, we assume a simple functional shape given by

$$R(x) = 1 + (R_0 - 1)\; e^{-x^2/\sigma_{df}^2} \tag{25}$$

with an e-folding distance σ_{df} after which the wind speed deficit is reduced to about one third.

In total the model thus has five parameters: the undisturbed wind speed at hub height upstream U, the Obhukov length scale L in the background wind field, the mixing length scale amplification factor Φ^{hub}, and the e-folding distances σ_{turb} and σ_{df}.

Fig. 8 shows two simulations with different choices for these parameters. Fig. 8a,b are the respective downstream profiles of u_* and Fig. 8c,d show vertical wind profiles at three different locations upstream and downstream. The friction velocities were computed by inserting the Charnock equation for z_0 in the respective profile equations and then solving the resulting implicit equation for u_* for a given wind speed at hub height. As one can see, the model is able to reproduce an increase in friction velocity values immediately behind the turbine for stable conditions with $L = 50$ m (Fig. 8a,c). After the turbulence is dissipated, u_* drops and finally recovers to the original value. For a more unstable situation with $L = 200$ m (Fig. 8b,d), the mixing mechanism is less effective and the friction velocity shows a drop downstream the OWF. Based on this model it is now clear that the occurrence of bright features downstream the turbines is favoured by stable conditions upstream, because in this case the mixing will lead to particularly strong increases of wind speeds at lower levels (Fig. 8c,d).

The model was fitted to observations using a standard cost function approach. In addition to the SAR observations, measurements from the nearby FINO-1 platform were used. Denoting the wind speed measurements at 50 m and 100 m height taken at FINO-1 by U_{50}^{FINO1}, U_{100}^{FINO1} the cost function is of the following form:

$$\begin{aligned} &J(U, L, \Phi^{hub}, \sigma_{turb}, \sigma_{df}) = \\ &\int_0^{x_f} W_x \left(u_*^{SIM}(x) - u_*^{SAR}(x)\right)^2 dx \\ &+ W_{50}\,(U_{50}^{FINO1} - U_{50}^{SIM})^2 + W_{100}\,(U_{100}^{FINO1} - U_{100}^{SIM})^2 \end{aligned} \tag{26}$$

The functions W_x,W_{50} and W_{100} are supposed to control the relative weighting of the observations in the minimisation process. In order to give the FINO-1 observations and the SAR measurements about equal weight we used $W_x = 1$ and $W_{50} = W_{100} = 0.001$.

Fig. 9 shows the friction velocities estimated from two Sentinel-1A scenes (blue curves) compared to the fitted empirical model results (red curves) for 22 May (Fig. 9a) and 30 October, 2015 (Fig. 9b). The approach to estimate friction velocity from SAR as described in Section IV A was applied. Because we do not have a special GMF for conditions of mechanically generated turbulence available, CMOD5.N was used in this context as well. One can see that the model is able to capture the main features of the observed downstream profile. The case from 22 May represents a stable situation (see table III), in which the model reproduces an increase in friction velocity within the first kilometers downstream. On 30 October the conditions were unstable and the friction velocity shows the expected downstream drop in friction velocity both in the observations and the model. There are different factors that can explain small scale variations of the wind speed deficit that cannot be captured by the model as seen about 30 km downstream in Fig. 9a. The one-dimensional approach used in the model has of course limitations, because in reality there are also lateral wind variations across the wake, which are very complex, because they are for example associated with the interaction of wakes behind different parts of the wind park[15]. Due to the applied averaging process some of these lateral variations can affect the SAR derived one-dimensional deficit curves discussed here. In addition the method to estimate the background wind field can introduce some noise in cases, where the background wind speeds have lateral (across wake) variations.

We are aware that alternative explanations for the observed bright features could be considered. For example, offshore turbines are an obstacle for the airflow and hence one can expect a "blockage" effect related to mass conservation, which can lead to acceleration of the air below hub height[17]. However, we favour the presented theory of increased downward momentum flux for two reasons:

- The large eddy simulations (LES) we found in the literature (e.g.,[17]) do not show blockage effects over the distance observed here (10 km).

- According to the scientific literature[15] the wake generated by the turbines should hit the water after about 10 rotor diameter (e.g., 1 km). This means the air below hub

height will be strongly affected by the turbulence from above and a blockage effect further downstream is hard to imagine.

Because of the relatively simple analytical expressions used to describe the wind profiles, the model is of course not able to describe the detailed airflow around the turbine blades. This would require further assumptions about turbulence that could be included in future extensions of the model. The other simplification that should be mentioned is that the law of the wall assumption with growing mixing length at higher altitudes is only applicable in the Prandtl layer, which is dominated by vertical momentum fluxes. It is well known that with the increasing height, modern wind turbines are often at least partly inside the Ekman layer, which is more dominated by Coriolis force and less by vertical mixing. Unified models to describe the transition between the different layers are the subject of ongoing research[57].

VII. SUMMARY AND CONCLUSIONS

In this study cases of isolated wakes and superimposed wakes behind the AV windpark are investigated. The statistical analysis is based on 23 SAR scenes acquired by TerraSAR-X and Sentinel1-A. The study of isolated wakes ("AVa") and superimposed wakes ("AVa+") shows evidence of wake effects reaching more than 30 km and 60 km downstream respectively. For the first time, a clear statistical relationship between the wake length and stability has been found for the location of the OWP Alpha Ventus based on the analysis of satellite data and insitu measurements. The wake length is stability-dominated and the wake intensity is more dependent on wind park configuration. The more stable the atmosphere condition is, the longer the wake gets. This is consistent with the earlier study of Hasager et al.[11], who analysed C-band SAR images and got wake lengths longer than 20 km downstream for near-neutral conditions. One important new result of the present study is a parametric model defining a quantitative relationship between stability and wake length for isolated wakes. This model can be useful for readers concerned with planning of offshore wind parks and as a reference for future studies.

In stable conditions, the maximum wake length was about 32 km for isolated wakes ("AVa") and 70 km for superimposed wakes ("AVa+"). Most of the scenes from "AVa", except the one from 30 October 2015, were acquired when Alpha Ventus was the only existing offshore wind park (OWP) in the area. The analysed SAR scenes from the data

set "AVa+" with superimposed wakes were acquired since 2015, when additional OWPs (e.g.,Borkum and Trianel) were erected. The downwind or upwind distance between the new OWPs and Alpha Ventus is not big (between 2 km and 10 km depending on direction). In Fig. 7b, the wake lengths from "AVa+" are not significantly longer than those from "AVa" for the same unstable range. In fact, in very unstable conditions, the wake is expected to be weak and short, so the influence of upstream OWPs do not affect much wakes downstream Alpha Ventus. However, in stable conditions the wake length is much longer for "AVa+". This clearly materializes the additional effects from neighbouring OWPs, that could be identified as a shadowing effects. The shadowing effects of one OWP to another for a small spacing can be significant and cause turbine fatigue loads in neutral and stable condition, because these conditions are favourable for the generation of long wake. On the contrary, the shadowing effect is a much smaller factor in very unstable conditions as the wake is very short. In contrast to the wake lengths, the analysis of the velocity deficit magnitude related to the wake intensity does not show a clear corelation with the stability conditions overall. However, for the "AVa+" cases, the velocity deficit magnitude for unstable situations seems to be higher than for stable ones.

The study also showed that there is a lot of scatter in the data and some longer wakes were in fact also found in unstable situations. Possible explanations for some unexpected observations were proposed, such as variations in the background wind field, or shadowing effects impacting the FINO-1 measurements. For the latter case the influence of the wake on the measurement platform in FINO-1 is more complex due to the increase of vertical mixing enhanced by the turbulence caused by the turbines. Also, the estimation of stability parameters is not straightforward and the fact that the SAR measurements are more correlated with the friction velocity at the sea surface rather than the wind speed at hub height leads to additional complications.

One unexpected behaviour of σ^0 that is found in about one quarter of the wake scenes was studied in more detail. In stable conditions the radar cross section is typically increased with respect to the background values within a dowstream distance of about 10 km. In more unstable conditions the cross section shows a rapid drop in cross section immediately downstream the OWF, which is more in accordance with expectations.

A model was proposed which explains this behaviour by an increased downward momentum flux behind the turbines due to mechanical turbulence generation. The model is

supposed to improve the understanding of the relationship between the SAR measurement, which is predominantly connected to the friction velocity and wind speeds at higher levels within the closer downstream regime, which is strongly affected by mechanically generated turbulence. It can thus help to avoid misinterpretations of SAR imagery following from naive application of standard SAR retrieval methods.

The future coverage of OWPs in German Bight around FINO-1 will further limit its usefulness for the estimation of freestream conditions. Systematic and continuous monitoring of expanding wind park installations are required. The study also showed a shortage of measurements closer to the surface. This will be of growing importance, because interaction processes between the atmosphere and the ocean are a critical factor for the understanding of OWPs impact on the environment.

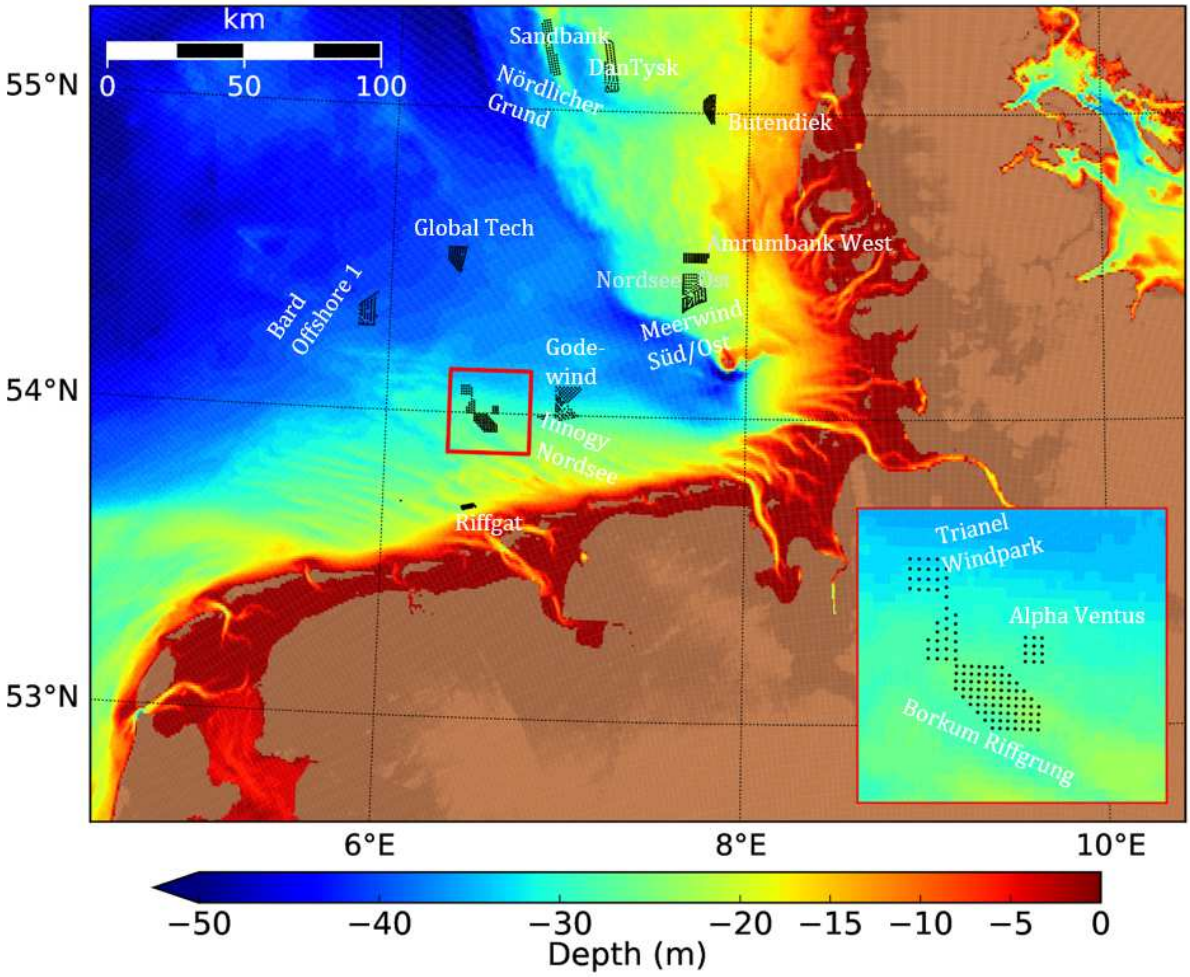

FIG. 1. Bathymetry of the German Bight with the locations of the major offshore wind parks (dated from June 2016) indicated by black dots. The red box indicates the area of interest around the offshore wind park Alpha Ventus.

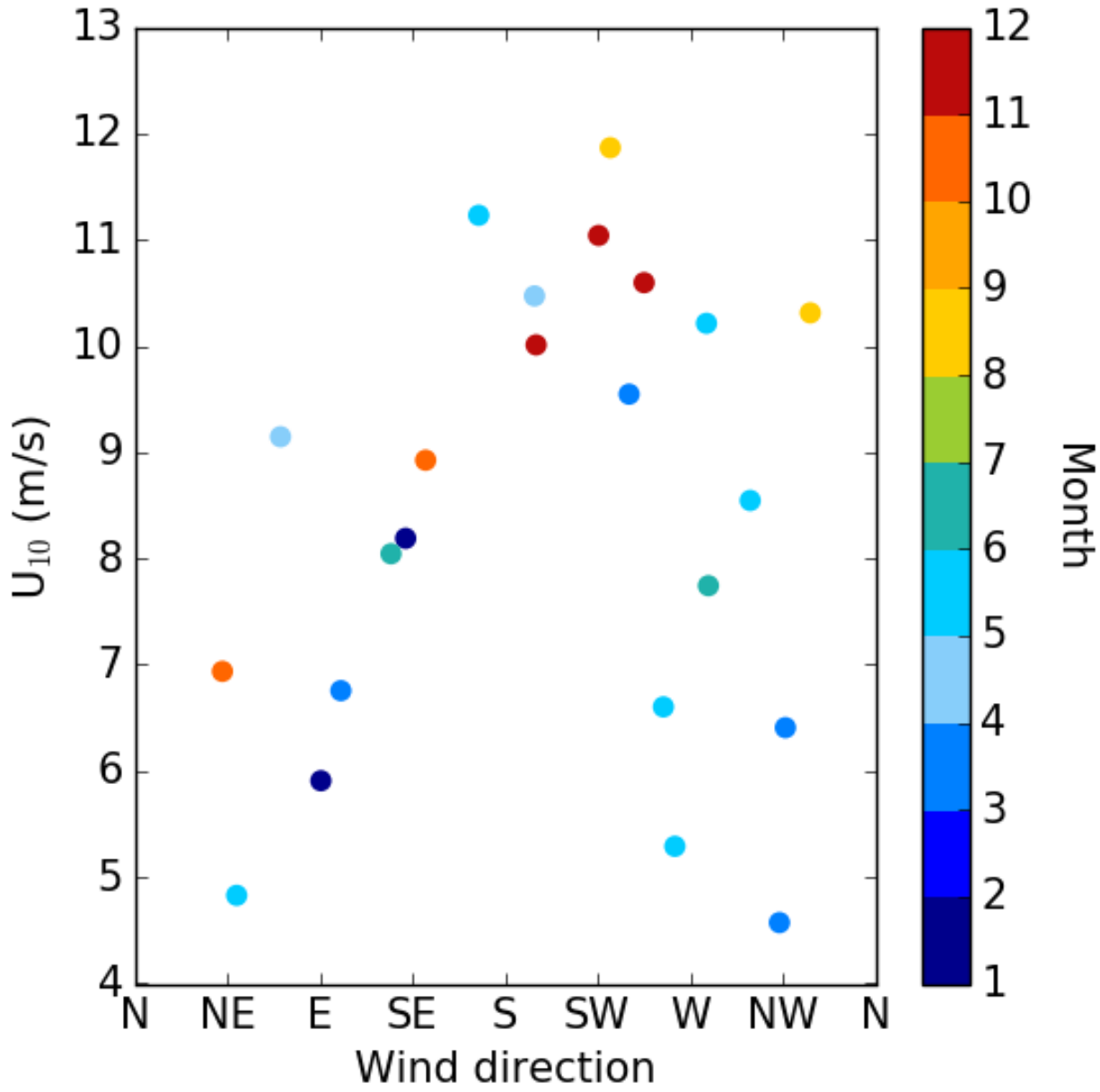

FIG. 2. Scatter plot of DWD model wind speed and wind direction for the analysed SAR scenes. The colors correspond to the month of the scene acquisition.

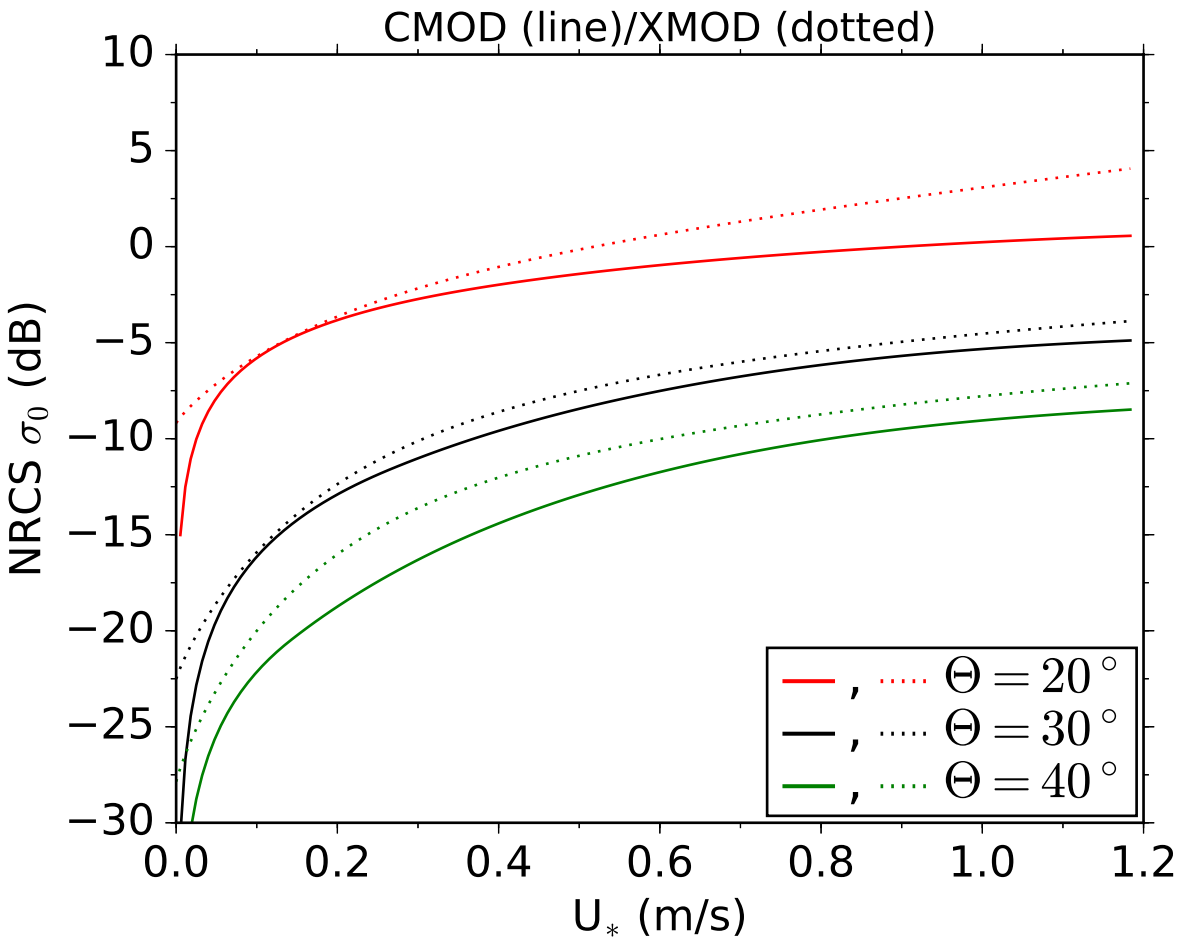

FIG. 3. NRCS as a function of the friction velocity u_* for C-band (solid line) and X-band (dotted line). The empirical CMOD and XMOD models were used for the simulation with incidence angles of 20°, 30° and 40°.

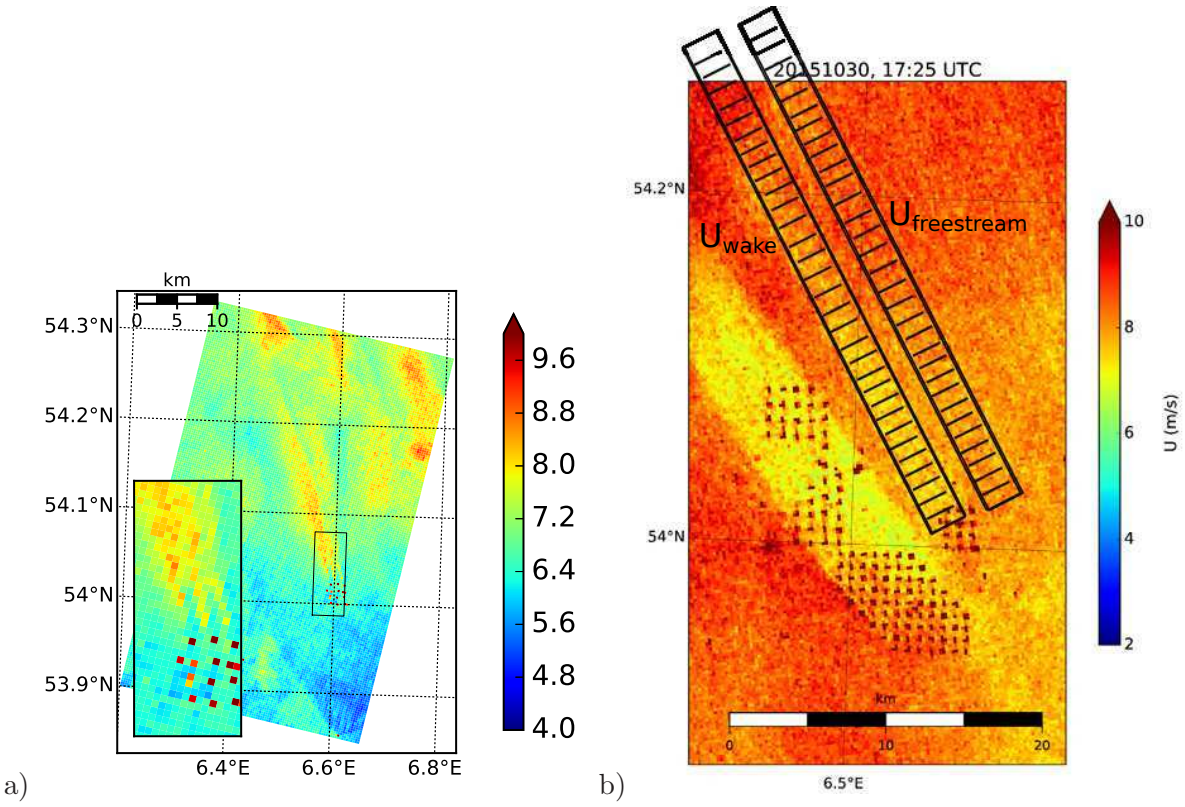

FIG. 4. (a) Example of background effects showing the increase of wind speed from South to North for an TS-X image from 10 May 2012, 05:59 UTC. b) Illustration of the method for wake length and V_d estimation based on two parallel transects applied to the Sentinel-1 image acquired on 30 October 2015, 17:25 UTC.

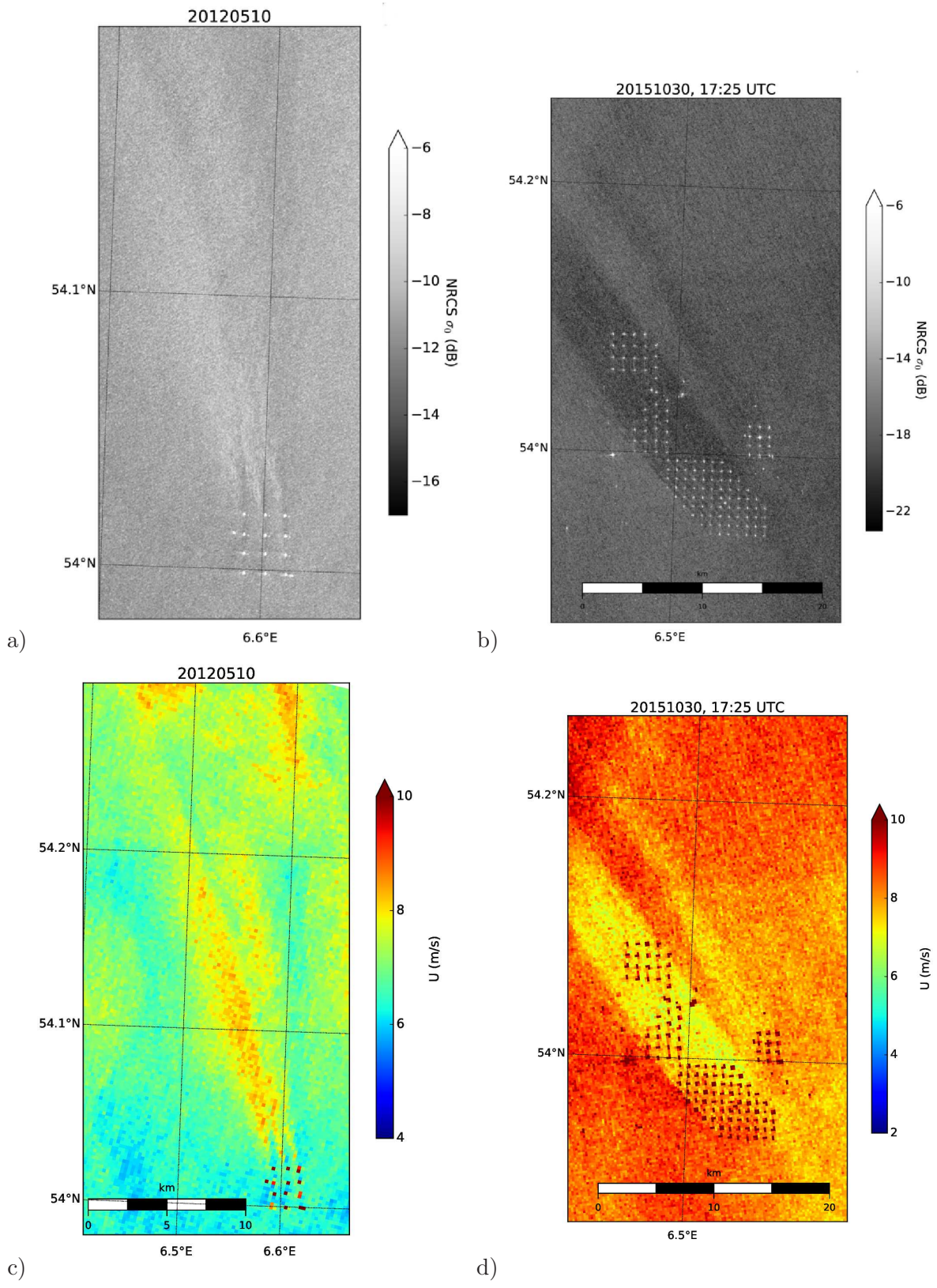

FIG. 5. (a,b): TS-X (a) and Sentinel-1 (b) scene showing an isolated wake behind AV acquired on 10 May 2012, 05:59 UTC (a) and on 30 October 2015, 17:25 UTC (b). (c,d): SAR derived U10 wind speed derived from the scenes shown in a) and b).

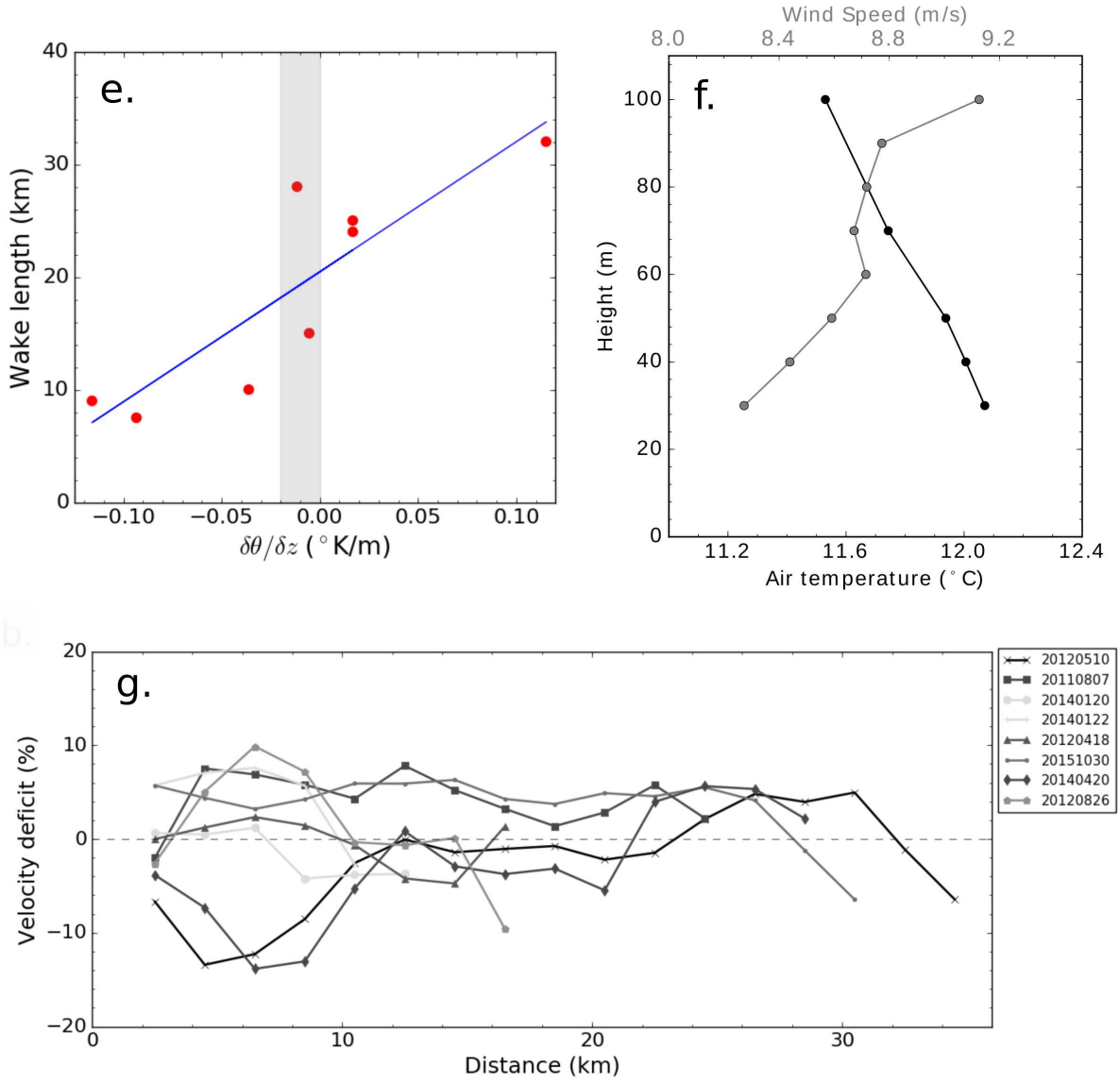

FIG. 5. (continued) (e) Scatterplot of thermal stability derived from FINO-1 insitu data versus SAR derived wake length for the "AVa" cases. (f) Vertical temperature (black) and wind speed (gray) profiles from FIN0-1 for 30 October 2016. (g) Velocity deficit curves for isolated wake cases with color indicating the stability: the darker color for more stable and gray color more unstable.

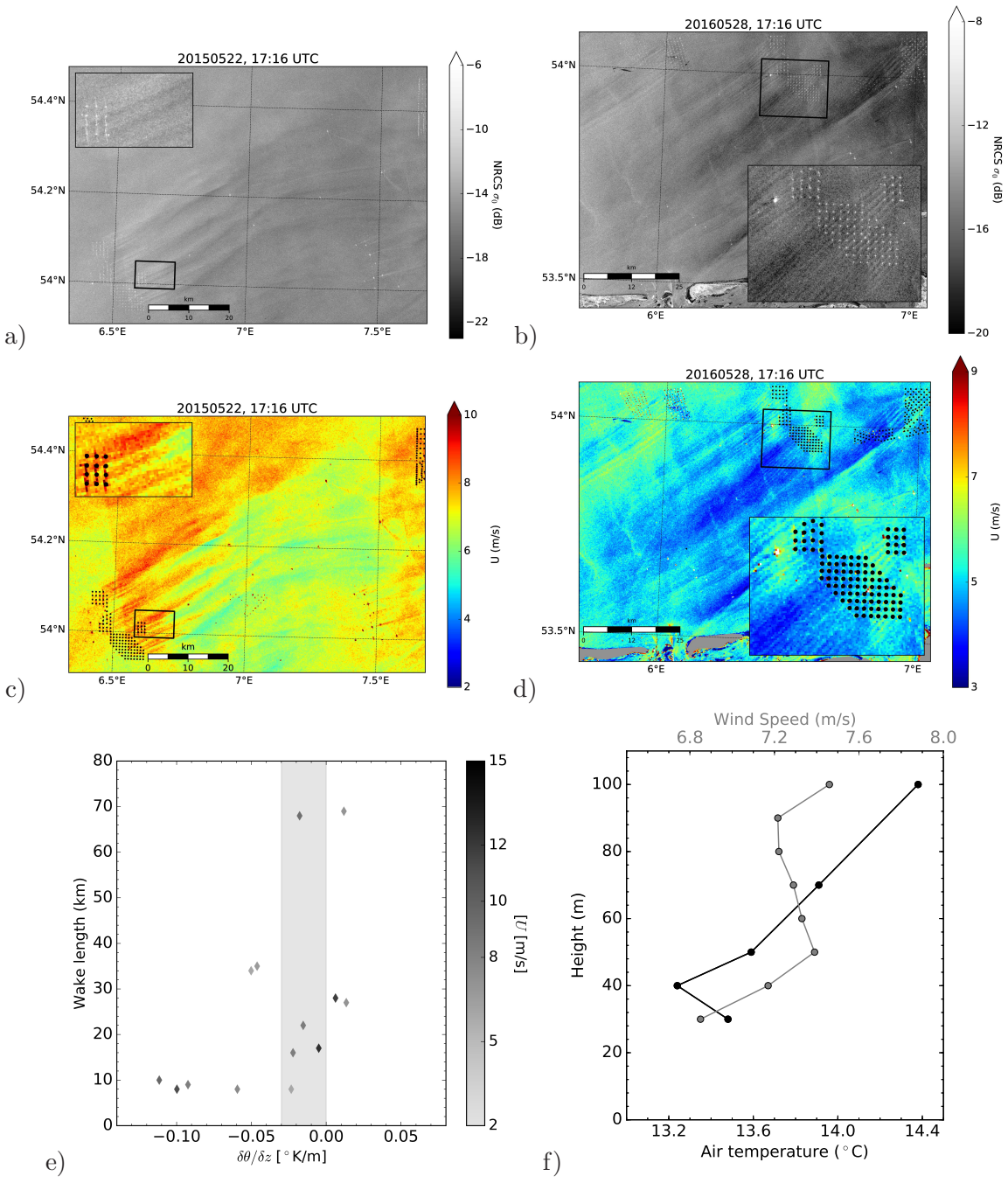

FIG. 6. (a,b): Two Sentinel-1 SAR scenes showing wake features behind the Alpha Ventus wind park acquired on 22 May 2015, 17:16 UTC (a) and 28 May 2016, 17:16 UTC (b). (c,d): SAR derived U10 wind speed derived from the scenes shown in a) and b). (e) Scatterplot of thermal stability derived from FINO-1 insitu data versus SAR derived wake length for the "AVa+" cases. (f) Vertical temperature (black) and wind speed (gray) profiles from FIN0-1 for 28 May 2016.

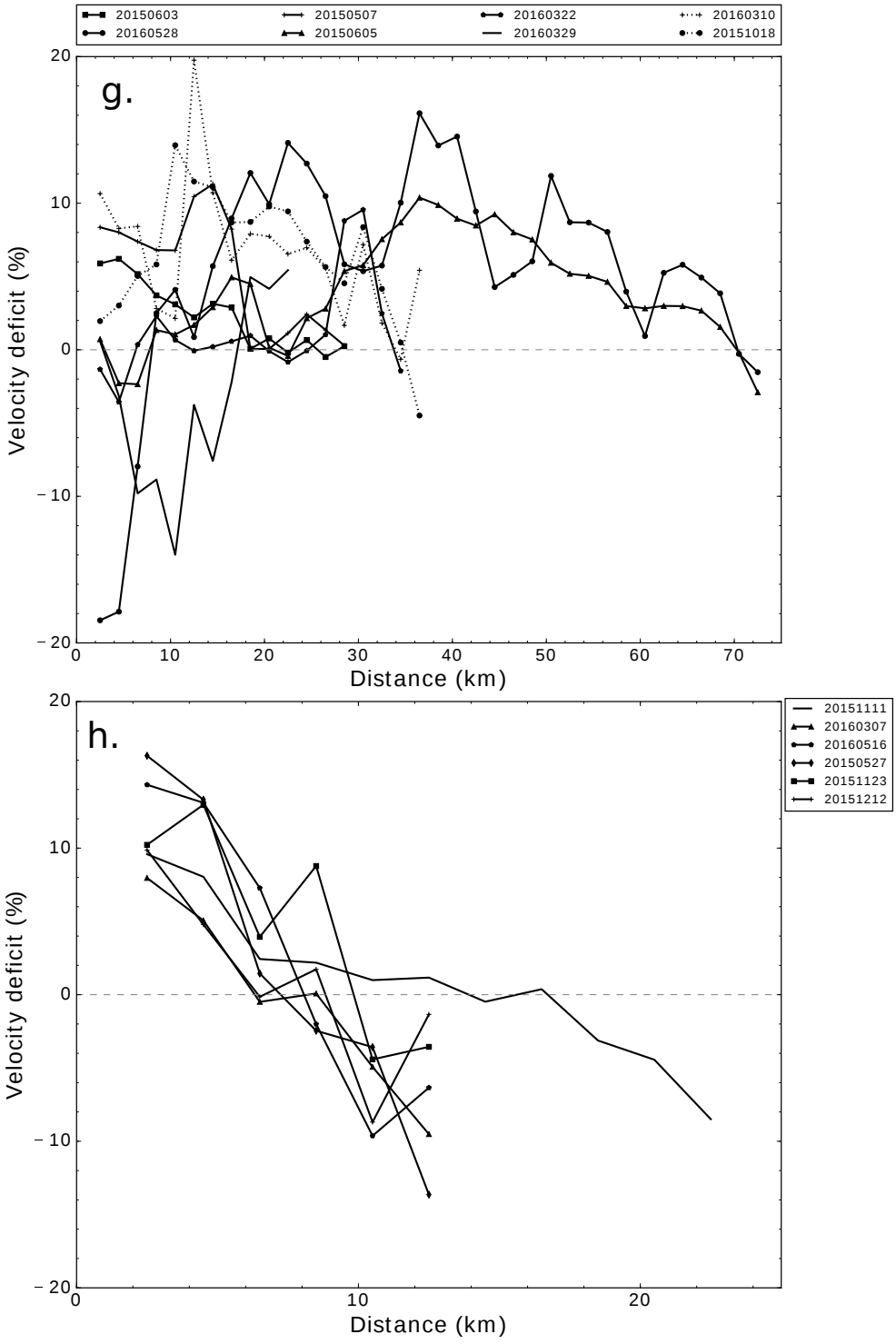

FIG. 6. (continued) Velocity deficit curves for longer (g) and shorter wakes (h) derived from SAR scenes for the "AVa+" cases. The curves in g) correspond to neutral and stable situations with the exception of the two gray curves, which are in unstable conditions.

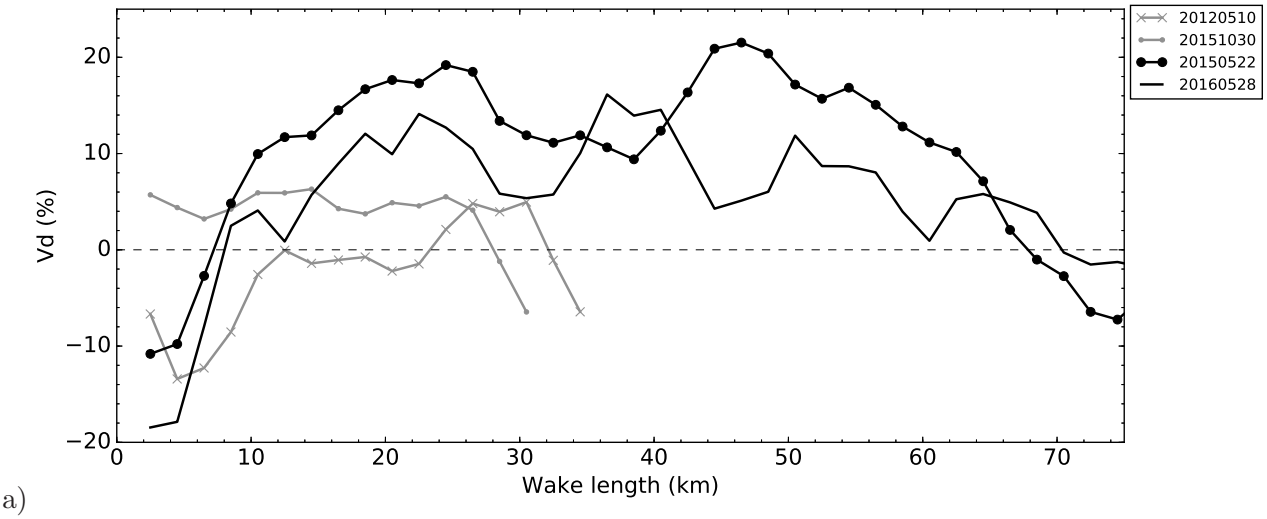

a)

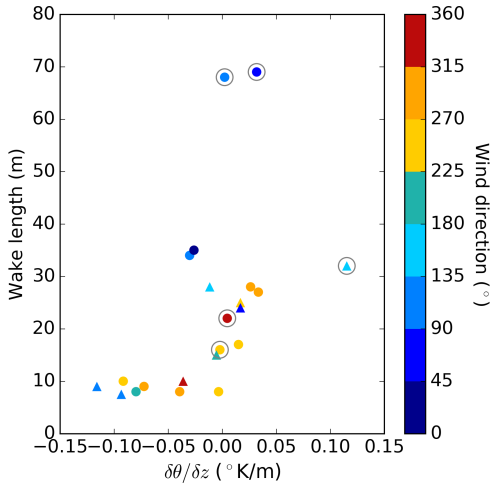

b)

FIG. 7. (a) Velocity deficit curves derived from the SAR images shown in Fig. 5 and Fig. 6. The grey curves (10 May 2012 and 30 October 2015) refer to the "AVa" situation, while the black curves (22 May 2015 and 28 May 2016) correspond to the more complicated "AVa+" cases. (b) Scatterplot of thermal stability derived from FINO-1 insitu data versus SAR derived wake length for both "AVa+" and "AVa" cases. Triangle symbols represent the cases in "AVa" and the dot symbols are from "AVa+". The colors represent the wind direction of each scene from DWD data. The circle represents the scenes, which show the increase of wind speed in the first kilometers downstream.

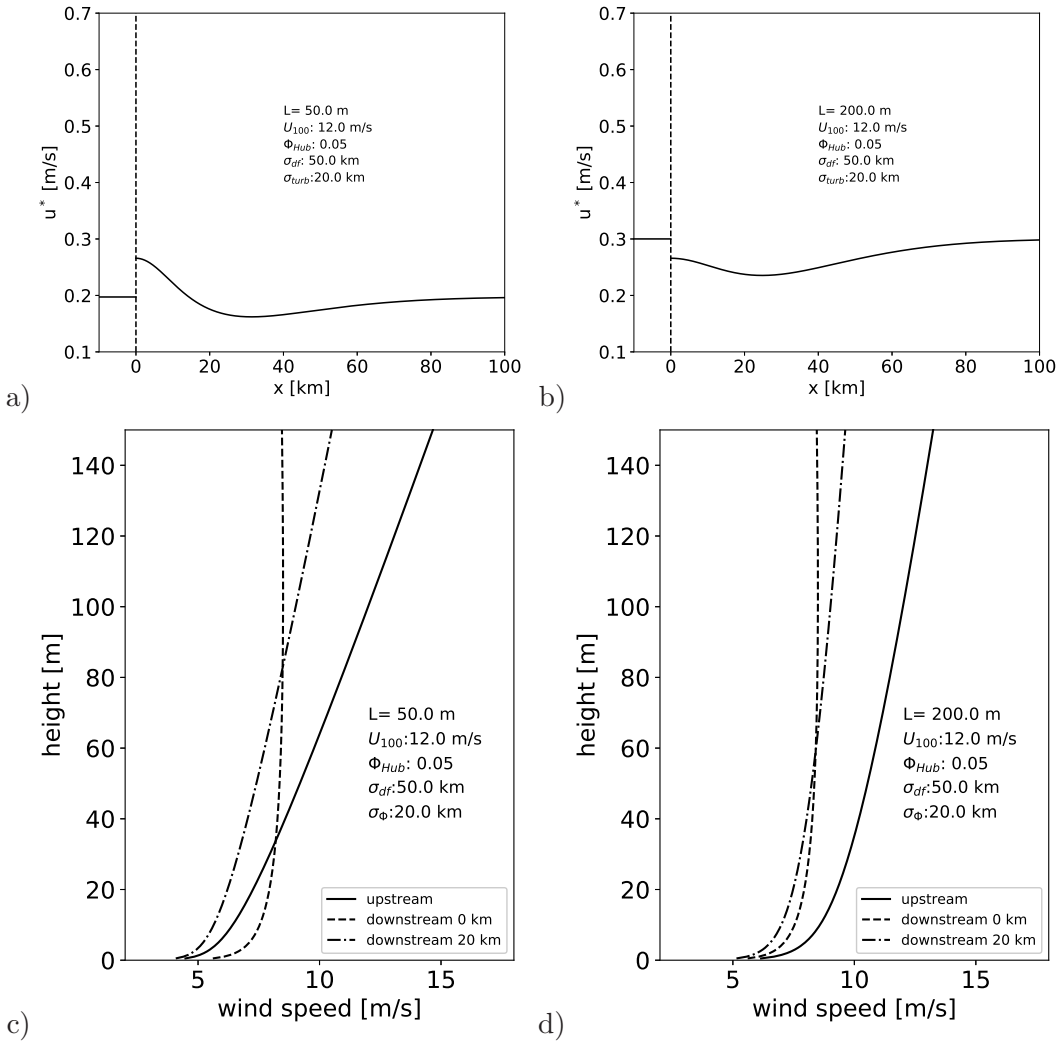

FIG. 8. (a,b) Downstream profiles of friction velocities estimated with the semi-empirical model using different parameter settings. (c,d) Corresponding vertical profiles upstream, directly behind turbine, and 20 km downstream estimated with the semi-empirical model using the parameter settings in a,b.

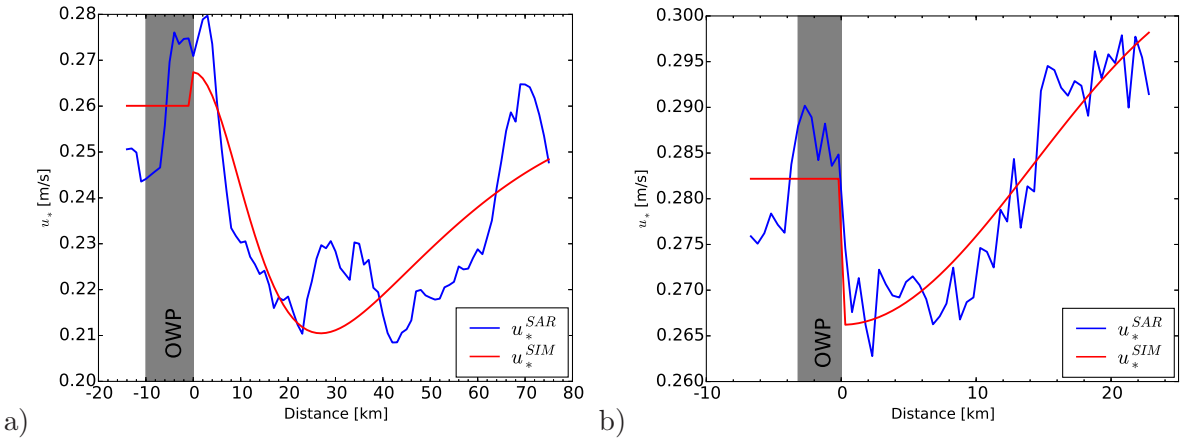

FIG. 9. Downstream profile of friction velocity obtained for the Sentinel-1a scenes acquired on 22 May (a) and 30 October (b), 2015 compared to the fitted empirical model (red curve) The gray shaded area indicates the position of the Alpha Ventus offshore wind park.

ACKNOWLEDGMENTS

This work was funded by the Federal Ministry for Economic Affairs and Energy (BMWi) in the framework of the project "Offshore Wind Park Far Fields (WIPAFF)" with project number 0325783C. TerrSAR-X data were kindly provided by the German Aerospace Center (DLR) in the framework of the science AO project COA3120. The FINO-1 platform is one of three offshore platforms of the FINO Project funded by the Federal Ministry for the Environment, Nature Conservation and Nuclear Safety (BMU). We also thank the European Space Agency (ESA) for making Sentinel-1 SAR data and the snap toolbox freely available.

REFERENCES

[1]IRENA (2014), "IRENA: A Renewable Energy Roadmap, Summary of Findings," Tech. Rep. (IRENA, Abu Dhabi, 2014).

[2]BMWi, "Zeitreihen zur Entwicklung der erneuerbaren Energien in Deutschland," Tech. Rep. (Bundesministerium für Wirtschaft und Energie, 2017).

[3]M. B. Christiansen and C. B. Hasager, Remote Sensing of Environment **98**, 251 (2005).

[4]X. Li and S. Lehner, Selected Topics in Applied Earth Observations and Remote Sensing, IEEE Journal of **6**, 1757 (2013).

[5]M. B. Christiansen and C. B. Hasager, Wind Energy **9**, 437 (2006).

[6]S. Emeis and S. Frandsen, Boundary-Layer Meteorology **64**, 297 (1993).

[7]S. Lehner, J. Horstmann, W. Koch, and W. Rosenthal, Journal of Geophysical Research: Oceans (1978–2012) **103**, 7847 (1998).

[8]S. Jacobsen, S. Lehner, J. Hieronimus, J. Schneemann, and M. Kühn, The International Archives of Photogrammetry, Remote Sensing and Spatial Information Sciences **40**, 959 (2015).

[9]M. Portabella, A. Stoffelen, and J. Johannessen, Journal Of Geophysical Research Oceans (2002), 10.1029/2001JC000925.

[10]C. B. Hasager, P. Vincent, J. Badger, M. Badger, A. Di Bella, A. Peña, R. Husson, and P. J. Volker, Energies **8**, 5413 (2015).

[11]C. B. Hasager, M. Nielsen, P. Astrup, R. Barthelmie, E. Dellwik, N. O. Jensen, B. H. Jørgensen, S. Pryor, O. Rathmann, and B. Furevik, Wind Energy **8**, 403 (2005).

[12]T. Schneiderhan, S. Lehner, J. Schulz-Stellenfleth, and J. Horstmann, Meteorological Applications **12**, 101 (2005).

[13]E. L. Petersen, N. G. Mortensen, L. Landberg, J. Højstrup, and H. P. Frank, Wind Energy **1**, 25 (1998).

[14]S. T. e. Frandsen and P. H. Madsen, Offshore Wind Energy in Mediterranean and Other European Seas. Resources, Technology, Applications (2003).

[15]S. Frandsen, R. Barthelmie, S. Pryor, O. Rathmann, S. Larsen, J. Højstrup, and M. Thøgersen, Wind energy **9**, 39 (2006).

[16]S. Emeis, Wind Energy **13**, 459 (2010).

[17]D. Yang, C. Meneveau, and L. Shen, Physics of Fluids (1994-present) **26**, 025101 (2014).

[18]A. Crespo, J. Hernandez, and S. Frandsen, Wind energy **2**, 1 (1999).

[19]D. W. Keith, J. F. DeCarolis, D. C. Denkenberger, D. H. Lenschow, S. L. Malyshev, S. Pacala, and P. J. Rasch, Proceedings of the national academy of sciences of the United States of America **101**, 16115 (2004).

[20]S. Baidya Roy, S. Pacala, and R. Walko, Journal of Geophysical Research: Atmospheres **109** (2004).

[21]G. Valenzuela, Radio Science **3**, 1057 (1968).

[22]S. Durden and J. Vesecky, IEEE Journal of Oceanic Engineering **10**, 445 (1985).

[23]F. Fois, Enhanced Ocean Scatterometry, Ph.D. thesis, Delft University of Technology (2015).

[24]S. Buckreuss and B. Schattler, IEEE Transactions on Geoscience and Remote Sensing **48**, 623 (2010).

[25]R. Torres, P. Snoeij, D. Geudtner, D. Bibby, M. Davidson, E. Attema, P. Potin, B. Rommen, N. Floury, M. Brown, and others, Remote Sensing of Environment **120**, 9 (2012).

[26]F. Saïd and H. Johnsen, IEEE Transactions on Geoscience and Remote Sensing **52**, 3980 (2014).

[27]A. Mouche and B. Chapron, Journal of Geophysical Research: Oceans **120**, 7195 (2015).

[28]K. Herklotz, DEWI Magazin **30**, 47 (2007).

[29]M. Borsche, A. K. Kaiser-Weiss, and F. Kaspar, Advances in Science and Research **13**, 151 (2016).

[30]A. Stoffelen and D. Anderson, Journal of Geophysical Research: Oceans (1978–2012) **102**, 5767 (1997).

[31]Ad Stoffelen, IEEE Journal of Selected Topics in Applied Earth (2017).

[32]M. B. Rivas, A. Stoffelen, J. Verspeek, A. Verhoef, X. Neyt, and C. Anderson, IEEE Journal of Selected Topics in Applied Earth Observations and Remote Sensing **10**, 2195 (2017).

[33]J. de Kloe, A. Stoffelen, and A. Verhoef, IEEE Journal of Selected Topics in Applied Earth Observations and Remote Sensing **10**, 2340 (2017).

[34]H. Hersbach, A. Stoffelen, and S. De Haan, Journal of Geophysical Research: Oceans **112** (2007).

[35]M. Portabella and A. Stoffelen, Journal of Atmospheric and Oceanic Technology **26**, 368 (2008).

[36]A. Verhoef, M. Portabella, A. Stoffelen, and H. Hersbach, "CMOD5. n-the CMOD5 GMF for neutral winds," Tech. Rep. SAF/OSI/CDOP/KNMI/TEC/TN/3, 165 (KNMI, De Bilt, Netherlands, 2008).

[37]X.-M. Li and S. Lehner, Geoscience and Remote Sensing, IEEE Transactions on **52**, 2928 (2014).

[38]M. Zuhlke, N. Fomferra, C. Brockmann, M. Peters, L. Veci, J. Malik, and P. Regner, in Sentinel-3 for Science Workshop, Vol. 734 (2015) p. 21.

[39]W. Koch, IEEE Transactions on Geoscience and Remote Sensing **42**, 702 (2004).

[40]Y. Zhao, X.-M. Li, and J. Sha, Journal of Geophysical Research: Oceans **121**, 6731 (2016).

[41]X. Li, L. Chi, X. Chen, Y. Ren, and S. Lehner, Journal of Geophysical Research: Oceans **119**, 4958 (2014).

[42]W. Koch and F. Feser, Monthly Weather Review **134**, 1505 (2006).

[43]I. Sandu, A. Beljaars, P. Bechtold, T. Mauritsen, and G. Balsamo, Journal of Advances in Modeling Earth Systems **5**, 117 (2013).

[44]A. Stoffelen, Journal of Geophysical Research: Oceans **103**, 7755 (1998).

[45]J. Vogelzang, A. Stoffelen, A. Verhoef, and J. Figa-Saldaña, Journal of Geophysical Research: Oceans **116** (2011).

[46]J. W. Antony, K. Schmidt, M. Schwerdt, D. Polimeni, N. Tous-Ramon, M. Bachmann, and G. C. Alfonzo, in EUSAR 2016: 11th European Conference on Synthetic Aperture Radar, Proceedings of (VDE, 2016) pp. 1–4.

[47]K. Schmidt, N. T. Ramon, and M. Schwerdt, in European Microwave Conference (EuMC), 2017 47th (IEEE, 2017) pp. 1175–1178.

[48]K. S. Hansen, R. J. Barthelmie, L. E. Jensen, and A. Sommer, Wind Energy **15**, 183 (2012).

[49]A. Grachev and C. Fairall, Journal of Applied Meteorology **36**, 406 (1997).

[50]Berliner-Wetterkarte, "Berliner Wetterkarte, Jg. 64, Nr. 96, ISSN 177-3984, www.berliner-wetterkarte.de," (2015).

[51]J. Garrat, The Atmospheric Boundary Layer (Cambridge University Press, 1994).

[52]A. J. Kettle, Journal of Wind Engineering and Industrial Aerodynamics **134**, 149 (2014).

[53]S. T. e. Frandsen, L. Chacón, A. Crespo, P. Enevoldsen, R. Gómez-Elvira, J. Hernández, J. Højstrup, F. Manuel, and K. Thomsen, "Measurements on and modelling of offshore

wind farms," Tech. Rep. (1996).

[54]F. Kinder, A. Westerhellweg, and T. Neumann, DEWI Magazin **42** (2013).

[55]A. Westerhellweg, B. Cañadillas, F. Kinder, and T. Neumann, in Journal of Physics: Conference Series, Vol. 555 (IOP Publishing, 2014) p. 012106.

[56]Z. Wang, A. Stoffelen, F. Fois, A. Verhoef, C. Zhao, M. Lin, and G. Chen, IEEE Journal of Selected Topics in Applied Earth Observations and Remote Sensing **10**, 2135 (2017).

[57]S. Emeis, Meteorological Applications **21**, 803 (2014).